Available online at www.sciencedirect.com
SCIENCE DIRECT®
ELSEVIER
European Journal of Mechanics B/Fluids 22 (2003) 155–166

# Mechanical load on a particle aggregate in mono-axial elongational flow

Christoph Hartmann *, Antonio Delgado

*Lehrstuhl für Fluidmechanik und Prozessautomation, Technische Universität München, Weihenstephaner Steig 23, 85350 Freising, Germany*

Received 9 January 2002; received in revised form 6 December 2002; accepted 15 January 2003

**Abstract**

Subject of the present contribution is the numerical simulation of the effect of a elongational flow field on a suspended particle-aggregate. The particle-aggregate consists of seven rigid spherical particles and is suspended in the flow field at low Re-numbers (Re = 0.01–0.1). The ratio of particle and fluid densities varies between 1 and 15. The velocity and pressure distribution is obtained from the numerical solution of the Navier–Stokes equation and the continuity equation based on finite volume methods. The particle motion is obtained from the Euler equation of motion for rigid bodies. A comparison of classical solutions with the result of the numerical simulation for a spherical particle shows a very good agreement. It can be shown, that the interaction of the aggregate with the fluid differs clearly from that of a spherical particle. Furthermore, it has been found that the magnitude of stresses on the aggregate surface is increasing with time monotonously. Shear stress is maximum on the outer parts of the aggregate. Normal stress takes on maximum values on the upstream and downstream oriented faces. The maximum pressure drop across the particle results in an extensional force which increases in time within the considered period.


*Keywords:* Elongational flow; Particle aggregate; Mechanical load

## 1. Introduction

In biotechnology and biology, various situations can be found where particles (e.g., rigid particles, micro-organisms, drops) are suspended in a fluid matrix. They interact with the matrix fluid on the level of chemistry, biology and mechanics. In the particular case of biological waste water treatment, aggregates of micro-organisms are cultivated in order to take advantage of their metabolistic activity for the purification of waste water in large activated sludge containers (bioreactors). The activated sludge flocs represent colonies of micro-organisms sticking together in an extra-cellular polymer substrate with an average typical length scale of around 500 μm. The flocs are formed by the micro-organisms in order to achieve better conditions for the survival in a hostile environment, see, e.g., [1,2]. Size and structure of the flocs can influence strongly the overall purification efficiency of the activated sludge bioreactor. At present, a relation between size, structure and flow induced stress on micro-organism-aggregates is investigated amply for shear flow, e.g., [3,4]. The effect of strain is investigated in a few contributions only, although it can lead to major modifications of the structure.

Based on this background the current paper deals with the interaction of aggregates as simplified flocs and elongational flow with a special interest on the stress distribution on the aggregates and their flow induced motion. The interaction between a straining fluid flow and suspended particles has sollicitated a considerable number of publications, which of the most important and recent ones are discussed subsequently.

* Corresponding author.
*E-mail address:* christoph.hartmann@wzw.tum.de (C. Hartmann).

0997-7546/03/$ – see front matter 
doi:10.1016/S0997-7546(03)00020-7

The largest group of contributions consider breakup of drops in elongational flow fields. The research activities can be classified in those which deal with Newtonian fluids, non-Newtonian fluids and drops with a solid membrane.

For the case that both drop and matrix are Newtonian fluids, Stone and Leal [5] examine drop deformation and break-up as a consequence of step changes in flow conditions. The authors show that the deformation prior to the change in flow conditions can result in a steady state deformation, a continuous large scale stretching or in a sudden break-up. The same authors consider in [6] the breakup of double emulsion droplets (globules) which appears to obey two distinct mechanisms. The first one represents a continuous extension of the globules; the second one is generated by a contact of inner and outer surfaces due to incompatible deformation of both interfaces.

The authors of [7] examine the motion and deformation of a single composite particle consisting of a Newtonian fluid surrounded by an elastic membrane in an extensional flow. A combined approach of experimental techniques and theoretical considerations yields an estimate of the elastic modulus of the membrane material for moderate deformations. Large strains lead to a permanent change of shape of the capsule.

In [8,9], drop deformation in uniaxial extensional flow is analysed under microgravity. The flow field is generated by sudden extension of a liquid bridge. The suspended drops are accelerated and elongated within less than 5 s. Typical deformation patterns like stretching and tip-forming are shown.

Other contributions investigate the behaviour of the extensional flow field in presence of drops when the fluids are non-Newtonian. In [10] the transient deformation of viscoelastic drops in either a viscoelastic or a Newtonian matrix at stationary extension is investigated. It is shown that viscoelastic drops lengthen less and recover quicker than Newtonian drops in a Newtonian matrix due to the influence of elastic stresses. The results are confirmed by the work in [11] by means of numerical simulation and are similar to those in [12] and [13]. Deformations are characterized as to be stronger in steady flows with the ends of the elongated drop more pointed. In transient startup and step like flows a pointed end shaped structure without necking in the midsection is observed.

A series of papers [14–16] reports about the deformation of visco-elastic and viscous drops exposed to non-stationary rotating extensional flow fields. Although the kinetics of the flow is much more complex than in pure extensional flow, stationary deformation modes can be observed as well as complex series of growth and collapse.

Concerning the effect of extensional flow on rigid particles, the following results are reported. The straining flow past a stationary rigid sphere is examined numerically in [17]. This contribution shows for pure straining flow, that the vorticity distribution around the sphere differs strongly from that of uniform flow. The re-circulation region appears at higher Re numbers, the separation angle and the reattachment length are strongly reduced.

The authors of [18] present a numerical investigation on the behaviour of a single sphere in elongational flow, in which results about particle motion and mechanical load are obtained. In the same context, experimental investigations are carried out in [19] on the behaviour of single ellipsoids in elongational flow. The experiments are conducted under micro-gravity. The authors examine especially the flow induced rotation of the ellipsoid, which aligns its principal axis according to the extension direction. Angular velocities of the order of magnitude of $10^3\ s^{-1}$ are observed.

Interaction of more complex structures like flocs and particle aggregates with elongational flow are subject of current research. In [20] the effect of shear and strain rates on the integrity of activated sludge flocs is investigated. It is shown, that strain is critical with respect to floc rupture. Flocs with a characteristic length in the range of 200 μm to 2000 μm are ruptured in moderate velocity gradients of $0.5\ s^{-1}$ to $1\ s^{-1}$ at break up forces of about 1 nN to 100 nN. In [21] it is shown, that flocs generated from precipitation products of Fe-III-salt can be destroyed by pure straining flow, provided that they are exposed to the straining load during a sufficiently long time period. In pure shear flow, the flocs tend to rotate and maintain their integrity.

The authors of [22] propose a two-dimensional modified DEM (mDEM) which determines iteratively the displacement of all individual particles of an aggregate within a time step using the total force and torque acting on each particle estimated from simplified drag laws. It is found that the model predicts the breakup process at least qualitatively. In [23], the mDEM method is further developed. The overestimation of the flow induced forces by using a Stokes flow analytical solution is corrected accounting for the influence of the neighbouring particles in the aggregate on the flow field. The comparison to experimental results suggests that the model is appropriate to simulate the behaviour of aggregates in fluids but cannot resolve the local stress distribution on the aggregate.

Resuming this overview of the current research on interaction between suspended particles (drops and aggregates) and elongational flow it can be stated, that

- in the case of deformable drops an analysis of stresses acting on the surface is not carried out explicitly. An interpretation of this configuration as a simplified biological cell system (either single cell or floc) is lacking the information about stress distribution on the surface as well as flow induced motion;
- in the case of rigid particles analyses about flow induced stresses and forces are given. Forces are mostly subdivided in their components in terms of history, added mass drag and lift. Due to the complexity of the fluid particle interaction these results remain limited to simple geometrical configurations like ellipsoids and spheres;

- the analysis of flow induced stresses on aggregates and flocs shows, that strain is critical for the integrity especially of biological flocs. Stresses on flocs given in the cited literature are determined again from simplified geometries as spheres or ellipsoids. The deformation of complex aggregates is considered on the basis of a strong simplification of the flow induced forces on the aggregates. A determination of stresses would be meaningless for these cases.

Consequently, the current contribution concentrates on small particle aggregates. The fluid flow as well as the flow induced motion of the aggregate are determined by direct numerical simulation of fluid and solid mechanics. This allows the determination of the stress distribution on the geometrically complex surface of the aggregate. Furthermore, the question whether the considered aggregate can be approximated by an equivalent spherical particle is going to be investigated. If this is shown to be possible, further analysis would not justify the use of computationally expensive numerical simulations.

The knowledge obtained form this work will facilitate the interpretation of experimental analyses on the deformation and motion of biological flocs. This initial study is going to be enhanced by further analyses on deformation of aggregates with a higher degree of complexity.

## 2. Problem description and solution method

### 2.1. Description of the physical problem

The considered aggregate is supposed to be approximately of the size of activated sludge flocs which ranges from 100 μm to 2 mm (see [20]). Typical strain rates observed in bioreactors are about 0.03 $s^{-1}$ to 0.3 $s^{-1}$ as obtained from own investigations [24].

The mathematical model is based on the assumption that a chemically inert incompressible newtonian fluid with constant properties is submitted to a uniform elongation at a constant rate $\dot{\varepsilon}$ along a given $z^+$-axis. Isothermal and gravity compensated conditions are assumed. The flow is supposed to be laminar.

The kinematics of pure uni-axial and stationary straining flow can be described in the form

$$v_x^+ = -\frac{1}{2}\dot{\varepsilon}x^+, \qquad v_y^+ = -\frac{1}{2}\dot{\varepsilon}y^+, \qquad v_z^+ = \dot{\varepsilon}z^+, \tag{1}$$

where $v_x^+$, $v_y^+$, $v_z^+$, are the dimensional velocity components in the dimensional $x^+$-, $y^+$- and $z^+$-direction respectively. An aggregate consisting of seven rigid spherical particles with the diameter $D$ is immersed in the fluid. It is assumed to be of a regular shape as depicted in Fig. 1. It is initially located on the $z$-axis in the centre of the computational domain. The bonding between the individual spheres is assumed to be rigid. The ratio $\Gamma$ between the density of the aggregate $\rho_S$ and the density of the fluid $\rho_F$ is given. The surface of the aggregate is supposed to be chemically inert, ideally wetting and impermeable to the liquid. Forces other than hydrodynamic are not taken into account in the current analysis.

### 2.2. Flow governing equations

The governing equations of fluid phase of the present problem are the Navier–Stokes equation and the continuity equation for an incompressible fluid. The equations are non-dimensionalised with the particle diameter $D$ as typical length scale and the reciprocal value of the elongation rate $\dot{\varepsilon}$ as a typical time scale. The velocity vector $\mathbf{v}$ is non-dimensionalized with $D\dot{\varepsilon}$, the dynamic pressure $p$ with $\rho_F D^2\dot{\varepsilon}^2$. Choosing $\mathbf{E}$ as the tensor of the deformation velocity, one obtains

$$\int_A \mathbf{v}\cdot\mathbf{n}\,\mathrm{d}A = 0, \tag{2}$$

$$\int_V \frac{\partial\mathbf{v}}{\partial\mathbf{t}}\,\mathrm{d}V + \int_V \mathbf{v}\cdot\nabla\mathbf{v}\,\mathrm{d}V = -\int_A \mathbf{p}\mathbf{n}\,\mathrm{d}A + \frac{1}{\mathrm{Re}}\int_V 2\nabla\cdot\mathbf{E}\,\mathrm{d}V. \tag{3}$$

The volume $V$ is surrounded by the area $A$ whereby $\mathbf{n}$ denotes the outward pointing normal unit vector. The Reynolds number is defined as $\mathrm{Re} = \rho_F\dot{\varepsilon}D^2/\eta$ where $\eta$ is the dynamic viscosity.

### 2.3. Equation of motion for the aggregate

For the motion of the aggregate the dimensionless Newton's Second Law

$$\Gamma n_p \frac{1}{6}\mathbf{a} = \mathbf{F}, \quad \text{where } \mathbf{F} = \int_{Ag} \mathbf{p}\mathbf{n}_{Ag}\,\mathrm{d}A - \int_{Ag} \boldsymbol{\tau}_{Ag}\cdot\mathbf{n}_{Ag}\,\mathrm{d}A, \tag{4}$$

and has to be integrated in time. $\Gamma$ represents the ratio between the particle density $\rho_S$ and the fluid density $\rho_F$. The number of particles composing the aggregate is denoted $n_p$, **a** represents the acceleration of the aggregate and **F** is the vector of the resulting force on the aggregate. It is obtained from an integration of the pressure and the tensor of the viscous stresses $\boldsymbol{\tau}_{Ag}$ over the aggregate surface $A_g$. Other forces such as gravitational or electrostatic forces are not accounted for at present. The rotation of the aggregate is taken into account by the equation for the conservation of the angular momentum. It is convenient to transform this equation to a frame of reference defined by the principal axes of the inertia tensor of the aggregate since the eigenvalues of the inertia tensor are constant in time. The three symmetry axes of the particle coincide with the principal axes in this particular case. One obtains the Euler equations of solid mechanics

$$\Theta_1 \cdot \dot{\omega}_1 - (\Theta_2 - \Theta_3)\omega_2\omega_3 = M_1, \tag{5}$$

$$\Theta_2 \cdot \dot{\omega}_2 - (\Theta_3 - \Theta_1)\omega_3\omega_1 = M_2, \tag{6}$$

$$\Theta_3 \cdot \dot{\omega}_3 - (\Theta_1 - \Theta_2)\omega_1\omega_2 = M_3, \tag{7}$$

where $\Theta_i$, $\omega_i$ and $M_i$ $(i = 1, 2, 3)$ are the principal moments of inertia, the vector components of the angular velocity of the aggregate and the torque vector components respectively, given in the principal frame of reference.

### 2.4. Boundary conditions and initial conditions

On the surface of the computational domain, the fluid velocity is described by the non-dimensionalised form of Eq. (1) and the pressure distribution of the undisturbed flow field are prescribed. The pressure distribution is obtained from the integration of the differential form of the Navier–Stokes equation for the velocity field defined by Eq. (1). It is given in non-dimensional form through

$$p(x, y, z) = C - \frac{1}{8}\left(x^2 + y^2\right) - \frac{1}{2}z^2, \tag{8}$$

where $C$ is an arbitrary constant chosen to be zero in the present case and $x$, $y$ and $z$ are the non-dimensional Cartesian coordinates. By successive increase of the size of the computational domain, it has been made sure, that the flow field is undisturbed close to the boundaries of the computational domain.

The aggregate is initially at rest. On the surface of the aggregate, the velocity of the fluid is set equal to the aggregate velocity. The pressure gradient is supposed to have a zero component normal to the surface of the aggregate.

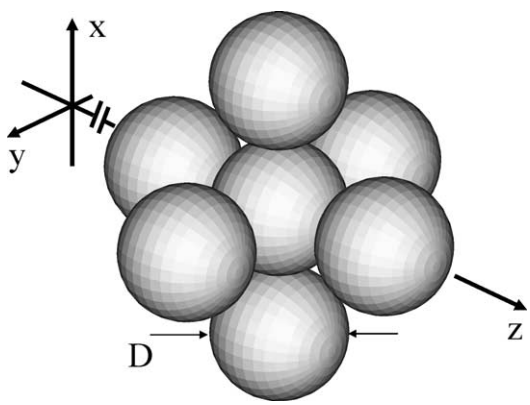


Fig. 1. Characteristics of suspended aggregate.

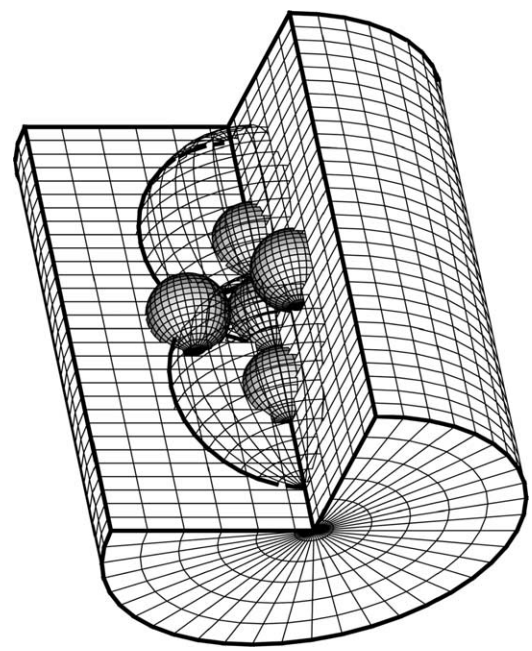

Fig. 2. Arrangement of computational grids.

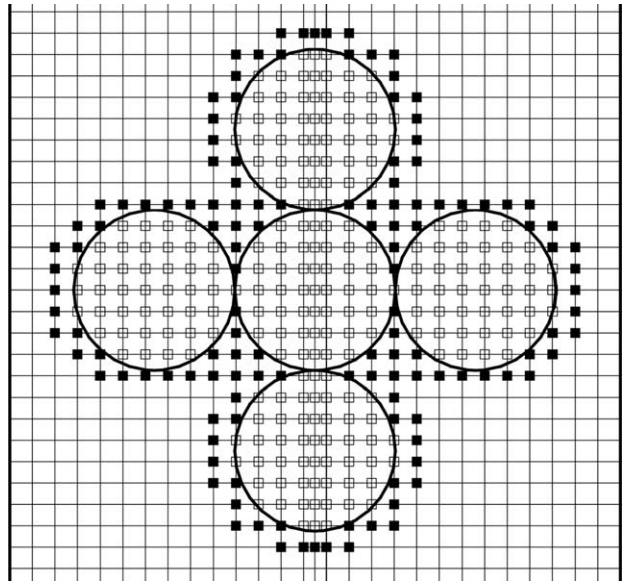

Fig. 3. Hole points and fringe points in the Chimera grid.

### 2.5. Numerical approach

The flow governing equations are solved with a cell centred finite-volume scheme. The spatial derivatives are approximated by central differences of second order accuracy. The pressure field is obtained from the solution of a Poisson equation, which is derived from the continuity equation, resulting from the definition of a "pressure correction" potential function [25]. The time integration scheme is the Crank–Nicholson scheme. The system of discrete equations is solved using the alternating direction implicit (ADI) method [26] enhanced by a GMRES-method [27].

A three-dimensional overlapping (Chimera) grid scheme [28] is applied in order to discretise the geometry of the aggregate. Therefore, eight independent grids are generated. One major grid represents the cylindrical geometry of the considered fluid volume. The seven minor body fitted grids define a close region around each of the seven spherical particles forming the aggregate. Fig. 2 shows the arrangement of the grids in proximity to the aggregate.

The typical Chimera scheme includes two major steps. At first, so called holes and fringe points are determined in both the major mesh and in the body fitted meshes for the spherical particles. As illustrated in Fig. 3, the holes (hollow squares) are the points in the major mesh where the rigid body is located. These points are excluded from the solution procedure. Fringe points (filled squares) are used in order to exchange data between two different meshes. Since the grid points of major and minor meshes are not coinciding a tri-linear interpolation procedure is applied in order to exchange the data. The present investigation deals with a time-dependent problem. Therefore, the evaluation of holes and fringe points has to be repeated after each time step.

The equations of motion for the particle-aggregate are solved in the following way. At first, normal and tangential stresses are computed from the viscous stresses and the pressure on the surface of the aggregate. Then, the resulting force and torque vectors are obtained from integration. The torque vector is then transformed to the coordinate system defined by the principal axes of inertia of the aggregate. By explicit time integration of Eqs. (4)–(7), the new aggregate velocity and the new position are obtained. Further details of the numerical schemes can be found in [29,30].

## 3. Results and discussion

The computational domain represents a coaxial cylindrical fluid element with the length $L$ which has been varied for different cases between $15D$ and $30D$. The radius $R$ of the domain has also be varied between $9D$ and $18D$. The results, especially particle trajectory and velocity, did not show any dependence on the dimension of the computational domain. Although it is known, that the domain of influence of a particle can extend far from its position in low-Re-number flows, in the current investigation, this observation could not be made. In the presented configuration the length $L$ is $15D$ and the radius $R$ is $9D$. The aggregate is initially positioned at $15/2D$.

The number of grid points of each mesh has been varied in order to obtain a grid independent solution. In the present results the resolution is $21 \times 44 \times 81$ for the main grid and $21 \times 32 \times 21$ for each of the minor grids (Fig. 2).

The Reynolds number is varied in the range of the between $\mathrm{Re} = 0.01$ to $\mathrm{Re} = 0.1$. This range has been chosen according to average values of the previously mentioned range of physical parameters of the problem. The density ratio is varied in the range between $\Gamma = 1$ to $\Gamma = 15$.

### 3.1. Comparison to classical solution

For the case of an individual spherical rigid particle exposed to uni-axial straining flow the present numerical technique has been compared to the classical equation of particle motion formulated by Basset, Boussinesq and Oseen [31]. Two different cases have been considered. One represents the case of $\mathrm{Re} = 0.01$ and $\Gamma = 5$, the second case is taken for $\mathrm{Re} = 0.1$ and $\Gamma = 1$. The $z$-coordinate of the particle trajectories are shown in Fig. 4. Both curves, the solution of the classical equation and the

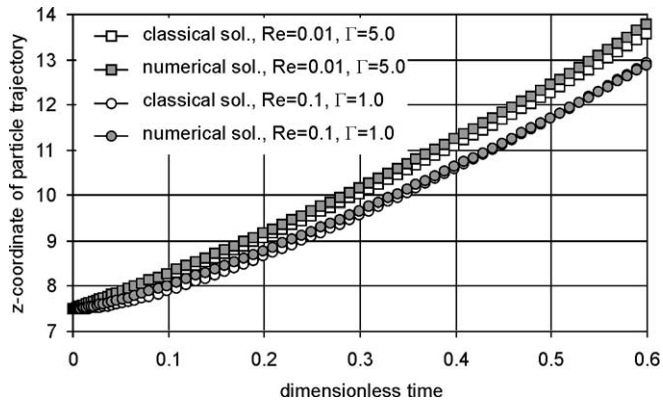


Fig. 4. Trajectories of isolated spherical particles.

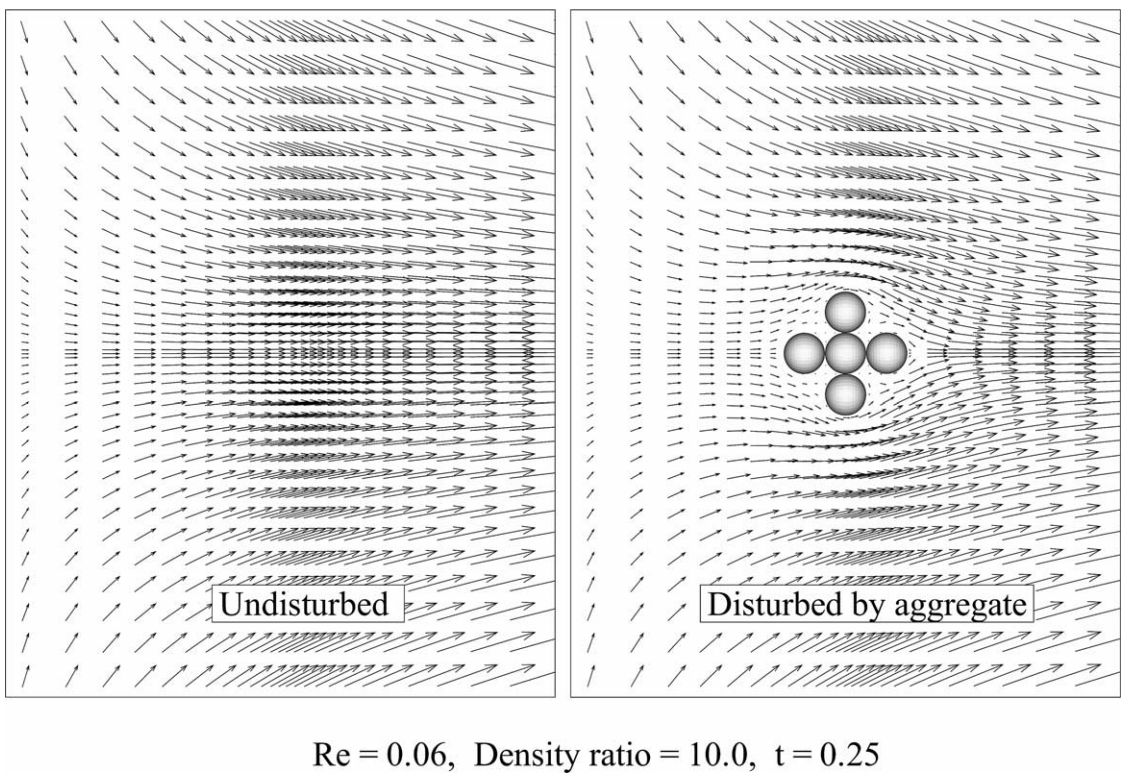


Fig. 5. Velocity field of undisturbed and disturbed flow.

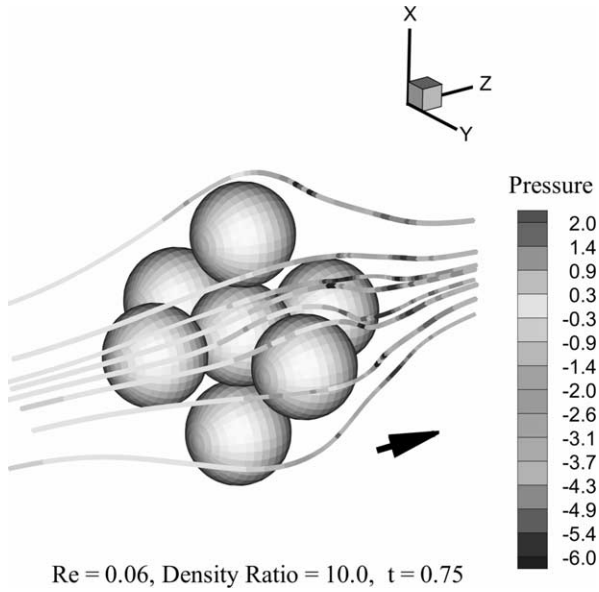


Fig. 6. Streamlines and pressure distribution.

solution of the numerical simulation are in excellent agreement. This shows the validity of the chosen numerical method for the investigation of the current problem.

### *3.2. Local flow field*

Fig. 5 shows in the right part the velocity distribution at $t = 0.25$ for $\mathrm{Re} = 0.06$ and $\Gamma = 10.0$ in a close region around the position of the aggregate. The undisturbed elongational flow is shown in the left part. The computed flow field corresponds to the analytical solution described by Eq. (1): the radial velocity components are constant at a constant radial distance from the central axis. With decreasing radius, the radial component approaches zero. The axial velocity component is increasing with an increasing $z$-coordinate. On the right part it can be found that the flow field is disturbed significantly by the existence of the aggregate within a distance of three times $D$ from the aggregate. Beyond this distance the velocity field is approaching the distribution of the undisturbed flow field.

The flow closely around the aggregate is illustrated by the streamlines in Fig. 6. The arrow indicates the direction of elongation. The local pressure is plotted as greyscale contour onto the streamlines. The streamlines around the extreme outer parts of the aggregate exhibit a strong curvature compared to those which are crossing the void volumes between individual particles of the aggregate. Maximum pressure gradients can be found on streamlines with a strong curvature while the pressure variations are smoother on less curved streamlines. This means, that the outer particles are exposed to higher pressure gradients, than those which are aligned along the central $z$-axis.

### *3.3. Stress distribution*

The pressure distribution on the surface of the aggregate is illustrated in Fig. 7. The numbers associated to the iso-lines represent different pressure levels given in the legend. Again, the arrow indicates the direction of elongation. It is found that a symmetrical distribution exists.

The maximum pressure can be observed on the upstream face of those particles, which are directly exposed to the flow field. On the central particle, the pressure is almost constant. The pressure reaches minimum values on the downstream face of the particles exposed directly to the flow field. The strongest pressure drop is acting on the downstream coaxially situated particle. Thus, this particle is exposed to the strongest extensional force resulting from the pressure drop.

Furthermore it can be observed, that the pressure decrease on the downstream face is significantly higher than the pressure increase on the upstream face. This is due to two reasons. Firstly, the pressure gradient magnitude of the undisturbed outer flow field increases linearly in the downstream direction. In addition to the pressure gradient of the (undisturbed) outer field, the local pressure drop across the aggregate contributes to the total gradient.

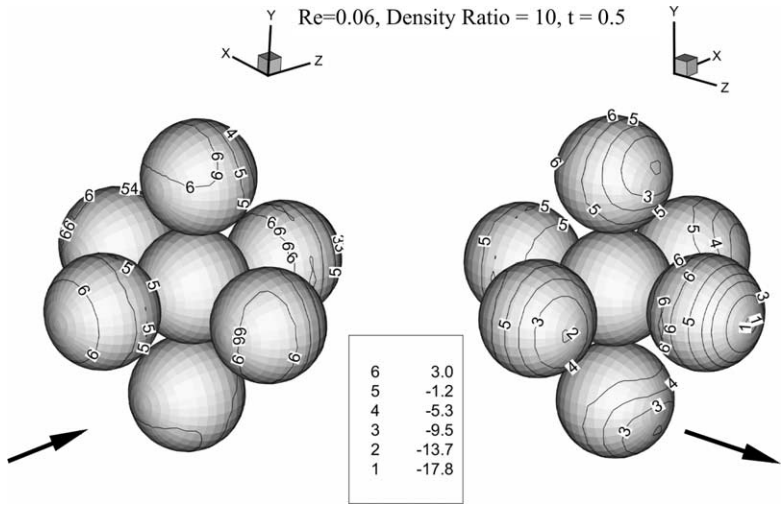


Fig. 7. Pressure distribution on surface of the aggregate.

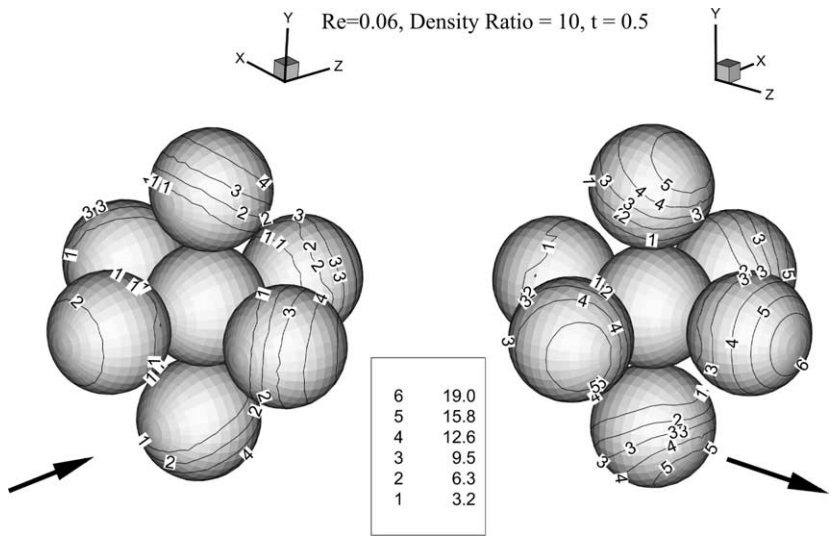


Fig. 8. Viscous stress distribution on surface of the aggregate.

The magnitude of the viscous surface stress vector on the surface of the aggregate exhibit also a symmetrical distribution as shown in Fig. 8. Again, the iso-line numbers represent different viscous stress levels given in the legend. In general, the viscous stresses on the outer parts of the aggregate are higher than those in the central part. Especially stresses on the coaxially situated downstream particle are three times higher compared to the upstream particle.

### *3.4. Influence of Reynolds number*

In Fig. 9, the development of the pressure drop across the surface of the aggregate is shown against dimensionless time for different Reynolds numbers. This quantity can be used as a criterion of the mechanical load, which is acting on the particle-aggregate in different flow situations. For a pure shear flow this quantity is constant [18]. In elongational flow, as shown in Fig. 9, it increases strongly with dimensionless time and obviously is unbounded. This means that extensional forces act on the aggregate which are increasing in time. They might lead to a decomposition as soon as these forces are stronger than the bonding forces of the aggregate.

For practical purposes, it can be concluded that the forces generated by an elongational flow on aggregates might be much higher than those generated in the case of pure shear flow. This conclusion is confirmed by [21].

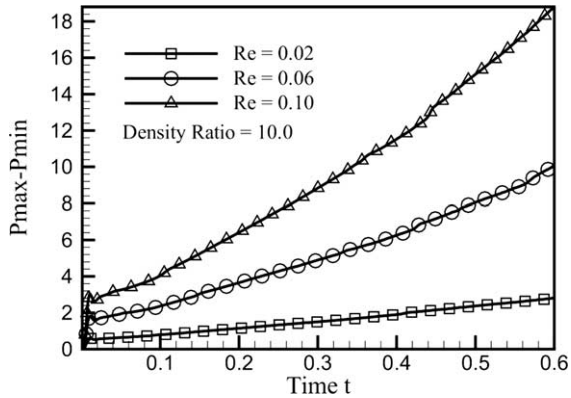


Fig. 9. Pressure drop over aggregate, effect of Re number.

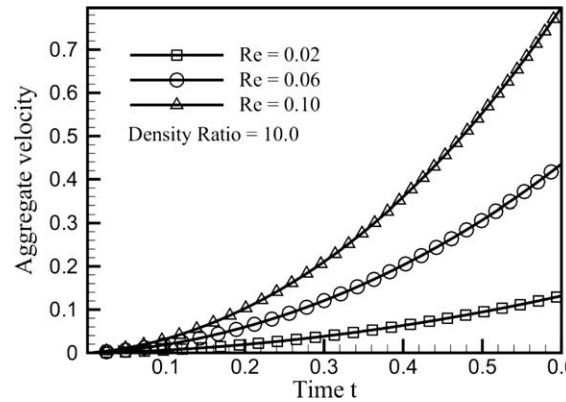


Fig. 10. Aggregate velocity, effect of Re number.

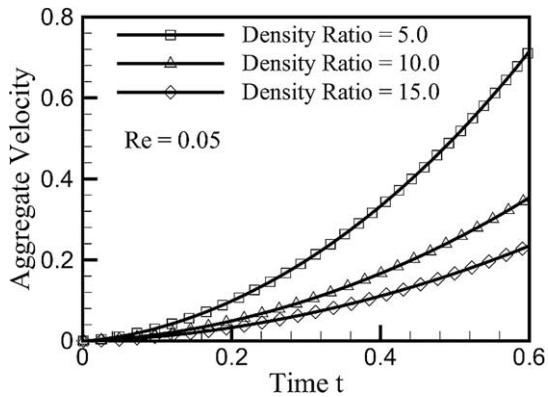


Fig. 11. Aggregate velocity, effect of density ratio.

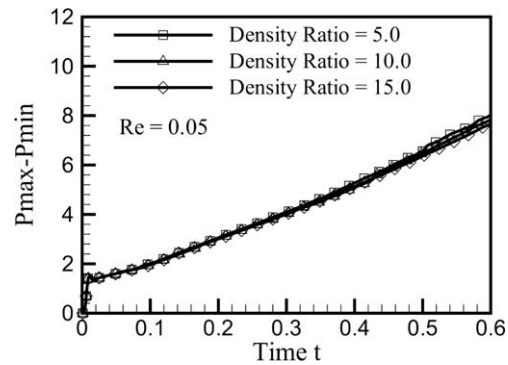


Fig. 12. Pressure drop over aggregate, effect of density ratio.

Furthermore, it can be observed, that the pressure drop increases also with increasing Re number. This is due to the stronger influence of inertia effects. While viscous damping of the aggregate motion reduces with increasing Re number, the aggregate is translated in the downstream direction. The pressure gradient magnitude of the outer flow field increases linearly along the downstream direction. Therefore, the resulting pressure drop across the aggregate becomes larger with an increasing displacement of the aggregate.

The aggregate velocity is illustrated in Fig. 10. It can be found that the velocities increase with the Reynolds number and with time. The aggregate exhibits a time-dependent acceleration which is growing with the Re number. This fact corresponds to the observations for the pressure drop, where an increase of the resulting force on the particle could be observed. Within the considered time period, the velocity is unbounded and the displacement of the aggregate is small. It does not exceed $0.2D$.

Rotation of the particle could be observed in none of the considered parameter cases, although no symmetry condition has been used. Even very small time steps which would allow to resolve chaotic rotations as observed by [32], did not reveal this kind of motion. Obviously, the flow induced torque resulting from numerically generated asymmetric load distributions remains small.

### *3.5. Influence of the density ratio*

Three different values (5, 10 and 15) are used for the density ratio $\Gamma$. As shown in Fig. 11, the aggregate velocity for different density ratios increases with time and is obviously unbounded.

An approximation of the velocity-time-curves by a polynomial of second order reveals that the acceleration is approximately constant for a given density ratio within the considered time period. Taking into account Newton's second law it can be stated that a constant acceleration on a body with a constant mass can only be induced by a constant force. This means in the current context, that within the considered time period the stresses on the particles are approximately constant in time.

Furthermore, it can be observed that the acceleration of the aggregates scales linearly with the density ratio. From this, one can conclude that the resulting force is the same for the three aggregates which have different masses. This can be explained

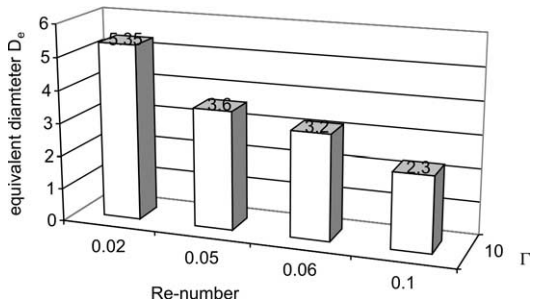


Fig. 13. Equivalent diameter of a spherical particle vs. Re number.

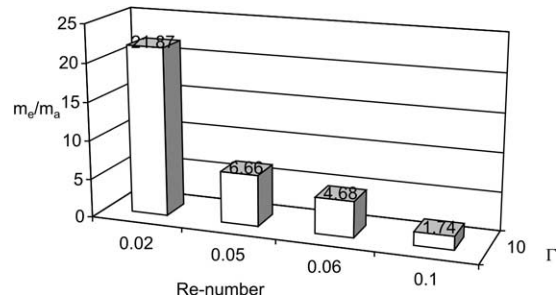


Fig. 14. Mass ratio between equivalent spherical particle and aggregate vs. Re number.

from the small displacement obtained for all density ratios. The velocity-distribution inducing pressure and viscous stresses on the aggregates is approximately the same in all three cases and will vary only for larger displacements, i.e., longer time periods.

This can also be seen from Fig. 12, where the pressure drop across the aggregate is shown for the different density ratios. The three curves are almost identical.

### *3.6. Equivalent particle diameter*

In order to investigate the question up to which extent the behaviour of the current aggregate agrees with that of a spherical particle, an equivalent particle diameter has been determined. The equivalent diameter is the diameter of a spherical particle, that exhibits the same kinematics as the aggregate if exposed to the same flow field. The equivalent diameter has been derived from the adaptation of the velocity characteristics of the classical solution for spherical particles to that of the current aggregate. The adaptation has been carried out by a variation of the equivalent particle diameter. In any subsequent consideration the material density of particles and aggregates is assumed to be the same.

In Fig. 13, it can be observed that the equivalent particle diameter decreases with increasing Reynolds number. The first conclusion to be drawn from this observation is that the aggregate in its specific form does not behave like an equivalent spherical particle in the considered range of the Reynolds number between $\mathrm{Re} = 0.02$ and $\mathrm{Re} = 0.1$; otherwise the equivalent particle diameter would remain constant within this range. At the lower bound the equivalent particle diameter is larger than the typical length of the aggregate ($3D$). At the upper bound ($\mathrm{Re} = 0.1$) the equivalent particle diameter is smaller than the typical length of the aggregate.

The ratio of the equivalent particle mass and the mass of the aggregate is shown in Fig. 14. It can be observed, that the mass of the equivalent spherical particle is 21.87 times larger than the mass of the aggregate at the lower bound of the Re-number range and still 1.74 times larger than the mass of the aggregate at the upper bound of the Re-number range.

Since both diameter and mass of the equivalent spherical particle decrease with increasing Re-number the following conclusion can be made. At low Re-number, the aggregate behaves like a larger spherical particle with a much larger mass. This means that the forces acting on the aggregate are comparably low, since the acceleration is low. With an increasing Re-number, the equivalent particle diameter decreases as well as its mass. This implies that the resulting force on the aggregate increases. An increasing Reynolds-number implies a stronger effect of inertia effects compared to viscous effects.

Furthermore, for the case of a constant Reynolds number $\mathrm{Re} = 0.05$, the equivalent particle diameter in dependence of a variable density ratio is shown in Fig. 15. It can be observed, that the equivalent particle diameter strongly increases with the density ratio. The diameter of an equivalent spherical particle is one for a density ratio of $\Gamma = 5$. Its mass is 0.14 times the mass of the aggregate. At a density ratio of $\Gamma = 15$, the diameter is almost equal to 4 and the mass ratio amounts up to 9.11. This strong increase implies that at low density ratios, the fluid field interacts more intensively with the aggregate. The fluid induced forces are sufficiently strong to induce the same acceleration that a spherical particle of the size of the particles composing the aggregate would have. Increasing the density of the aggregate yields to the situation that an equivalent spherical particle is slightly larger than the aggregate and its mass is much larger than that of the aggregate. This means that the induced acceleration decreases strongly. The flow induced forces lead only to a minor acceleration. This can again only be explained by the geometry of the aggregate which represents only a minor obstacle for the fluid flow.

## 4. Conclusions

In the present paper, a numerical simulation of the interaction of pure elongational flow and a suspended aggregate is presented with an emphasize on flow induced motion and spatial distribution of stress.

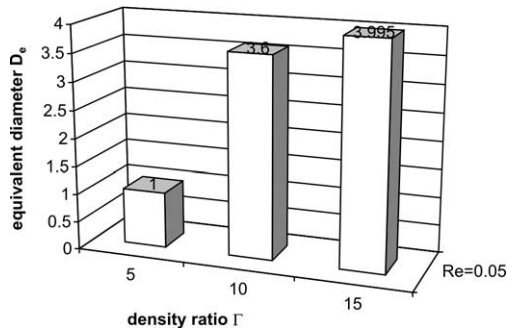


Fig. 15. Equivalent diameter of a spherical particle vs. density ratio.

It can be shown, that the maximum viscous stress on the surface of the aggregate, which is responsible for erosive damage, is present on the extreme outer particles of the aggregate. Minimum viscous stresses are observed on particles which are not exposed directly to the flow field.

The surface pressure distribution reveals a high load of the upstream and of the downstream located particles of the aggregate. While on the upstream particle the pressure is maximum, the downstream particle is exposed to minimum pressure. This implies an overall pressure drop across the aggregate which represents a resulting extensional force responsible for desintegration. The resulting force is increasing with time and is unbounded within the considered time period. In contrast to pure shear flow, where the mechanical load of the aggregate is time periodic but has a constant amplitude, the load in pure elongational flow is increasing monotonously and might reach the level of the bonding forces of the aggregate. It has to be subject to future work to analyse up to which extent this load can be disruptive. Due to the resulting force, the aggregate is accelerated in the downstream direction. It can be found that the velocity of the aggregate increases monotonously with time as well. Furthermore, it has been found, that the interaction between aggregate and surrounding flow field differs clearly from that of an equivalent spherical particle. In the considered range of Re-number and density ratio, the diameter of an equivalent spherical particle decreases strongly with an increasing Re-number and increases strongly with an increasing density ratio. This means, that the aggregate is influenced by the fluid flow to a minor extend at the lower bound of the Re-number range but is interacting in a more intensive way with a rising Re-number. Future work will be dedicated to the analysis of the fluid particle interaction of more complex aggregates. Especially the flow induced deformation up to breakup will allow to determine in combination with experimental techniques the strength of flocs and will allow to provide a mechanism to influence the size distribution of flocs.

## References

[1] W.G. Charaklis, P. Wilderer (Eds.), Structure and Function of Biofilms, Wiley, New York, 1989.
[2] J. Wingender, T.R. Neu, H.C. Flemming, What are bacterial extracellular polymeric substances?, in: J. Wingender, T.R. Neu, H.C. Flemming (Eds.), Microbial Extracellular Polymeric Substances, Springer, Berlin, 2000, pp. 1–15.
[3] W.G. Characklis, M.H. Turakhia, N. Zelver, Transport and interfacial transfer phenomena, in: W.G. Characklis, Marshall (Eds.), Biofilms, Wiley, New York, 1990, pp. 265–340.
[4] L.H. Mikkelsen, K. Keiding, The shear sensitivity of activated sludge: an evaluation of the possibility for a standardised floc strength test, Water Res. 36 (12) (2002) 2931–2940.
[5] H.A. Stone, L.G. Leal, The influence of initial deformation on drop breakup in subcritical time-dependent flows at low Reynolds numbers, J. Fluid Mech. 206 (1989) 223–263.
[6] H.A. Stone, L.G. Leal, Breakup of concentric double emulsion droplets in linear flows, J. Fluid Mech. 211 (1990) 123–156.
[7] K.S. Chang, W.L. Olbricht, Experimental studies of the deformation of a synthetic capsule in extensional flow, J. Fluid Mech. 250 (1993) 587–608.
[8] C.P. Berg, M. Dreyer, H.J. Rath, Drop deformation in uniaxial extensional flow fields in microgravity, Z. Angew. Math. Mech. 80 (3) (2000) 713–714.
[9] C.P. Berg, M. Dreyer, H.J. Rath, Pointed-droplets in uniaxial extensional flow, Z. Angew. Math. Mech. 81 (2) (2000) 279–280.
[10] R.W. Hooper, V.F. De Almeida, C.W. Macosko, J.J. Derby, Transient polymeric drop extension and retraction in uniaxial extensional flows, J. Non-Newtonian Fluid Mech. 98 (2–3) (2001) 141–168.
[11] R.E. Khayat, A. Luciani, L.A. Utracki, F. Godbille, J. Picot, Influence of shear and elongation on drop deformation in convergent–divergent flows, Int. J. Multiphase Flow 26 (1) (2000) 17–44.
[12] D.C. Tretheway, L.G. Leal, Deformation and relaxation of Newtonian drops in planar extensional flows of a Boger fluid, J. Non-Newtonian Fluid Mech. 99 (2–3) (2001) 81–108.
[13] H. Jong-Wook, L.G. Leal, An experimental study of drop deformation and breakup in extensional flow at high capillary number, Phys. Fluids 13 (6) (2001) 1568–1576.

[14] K. Sarkar, W.R. Schowalter, Deformation of a two-dimensional drop at non-zero Reynolds number in time-periodic extensional flows: numerical simulation, J. Fluid Mech. 436 (2001) 177–206.
[15] K. Sarkar, W.R. Schowalter, Deformation of a two-dimensional drop in time-periodic extensional flows: analytical treatment, J. Fluid Mech. 436 (2001) 207–230.
[16] K. Sarkar, W.R. Schowalter, Deformation of a two-dimensional visco-elastic drop at non-zero Reynolds number in time-periodic extensional flows, J. Non-Newtonian Fluid Mech. 95 (2–3) (2000) 315–342.
[17] J. Magnaudet, M. Rivero, J. Fabre, Accelerated flows past a rigid sphere or a spherical bubble: 1. Steady straining flow, J. Fluid Mech. 284 (1995) 97–135.
[18] H. Nirschl, A. Delgado, Simulation of particle behaviour in elongational flow, in: Proceedings of 1st International Symposium on food Rheology and Structure, Zurich, 1997, pp. 319–323.
[19] S. Arnold, A. Delgado, Untersuchungen zum Bewegungsverhalten einzelner Partikel in einer monoaxialen Dehnströmung, Jahrbuch 1998 der Deutschen Gesellschaft für Luft- und Raumfahrt Lilienthal-Oberth e.V. (DGLR), 1, pp. 485–495.
[20] M. Boller, S. Blaser, Particles under stress, Water Sci. Technol. 37 (10) (1998) 9–29.
[21] S. Blaser, The hydrodynamical effect of vorticity and strain on the mechanical stability of flocs, Ph.D. Thesis, Swiss Federal Institute of Technology Zürich, Zürich, Switzerland, 1999.
[22] K. Higashitani, K. Iimura, Two-dimensional simulation of the breakup process of aggregates in shear and elongational flows, J. Colloid Interface Sci. 204 (1998) 320–327.
[23] K. Higashitani, K. Iimura, H. Sanda, Simulation of deformation and breakup of large aggregates in flows of viscous fluids, Chem. Engrg. Sci. 56 (2001) 2927–2938.
[24] K. Debus, Numerischen Untersuchung zur Kugelhaufendurchströmung- Ansätze zur Berechnung strömungsbedingter Deformation verformbarer Körper, Ph.D. Thesis, TU München, 1997.
[25] R. Temam, The Navier–Stokes Equation, North-Holland, Amsterdam, 1977.
[26] G.I. Marchuk, Methods of Numerical Mathematics, Second edition, Springer, 1982.
[27] Y. Saad, M.H. Schultz, A generalized minimal residual algorithm for solving nonsymmetric linear systems, SIAM J. Sci. Statist. Comput. 7 (1986) 856–869.
[28] H. Nirschl, Mikrofluidmechanik – Numerische und experimentelle Untersuchungen zur Umströmung kleiner Körper., Ph.D. Thesis, Technische Universität München, Munich, Germany, 1994.
[29] S. Esterl, Numerische Simulation des Impuls- und Stofftransports in Festbett-Bioreaktoren, Ph.D. Thesis, Technische Universität München, Munich, Germany, 2001.
[30] H. Nirschl, Partikelbewegungen in Scherströmungen ohne und mit Berücksichtigung des Einflusses angrenzender Wände, Habilitation-Thesis, Technische Universität München, Munich, Germany, 1997.
[31] J.O. Hinze, Turbulence, McGraw-Hill, New York, 1975.
[32] A.L. Yarin, O. Gottlieb, I.V. Roisman, Chaotic motion of triaxial ellipsoids in simple shear flow, J. Fluid Mech. 340 (1997) 83–100.